DOI: 10.1002/chem.201001099

Bismuth-Doped Ordered Mesoporous TiO_2: Visible-Light Catalyst for Simultaneous Degradation of Phenol and Chromium

Shamaila Sajjad,[a] Sajjad A. K. Leghari,[a] Feng Chen,[a] and Jinlong Zhang*[a, b]

Abstract: A controllable and reproducible synthesis of highly ordered two-dimensional hexagonal mesoporous, crystalline bismuth-doped TiO_2 nanocomposites with variable Bi ratios is reported here. Analyses by transmission electron microscopy, X-ray diffraction, Raman, and X-ray photoelectron spectroscopy reveal that the well-ordered mesostructure is doped with Bi, which exists as Bi^{3+} and $Bi^{(3+x+)}$. The Bi-doped mesoporous TiO_2 (ms-TiO_2) samples exhibit improved photocatalytic activities for simultaneous phenol oxidation and chromium reduction in aqueous suspension under visible and UV light over the pure ms-TiO_2, P-25, and conventional Bi-doped titania. The high catalytic activity is due to both the unique structural characteristics and the Bi doping. This new material extends the spectral response from UV to the visible region, and reduces electron–hole recombination, which renders the 2.0% Bi-doped ms-TiO_2 photocatalyst highly responsive to visible light.

Keywords: bismuth · chromium reduction · mesoporous materials · phenol oxidation · photocatalysis

Introduction

Mesoporous materials with tunable pore structure and tailored framework composition are of great interest for broad applications ranging from adsorbent materials, separations, catalysis, energy storage, and biological conversions.[1–3] Among this family of materials, mesoporous titania is of particular interest because its semiconductor framework is photoactive, while its mesoporous channels offer larger surface area and enhanced accessibility. Such a unique combination provides a new platform for the design and fabrication of novel photoactive materials and devices, such as high-efficiency photocatalysts and photovoltaic devices.[4] To date, titania's low quantum efficiency has been limited due to its high bandgap (3.0–3.2 eV) in the UV range.[5] The utilization of mesoporous titania as a highly active photocatalyst thus remains challenging. Possible strategies toward overcoming this intrinsic limitation include doping titania with inorganic or metallic species, such as ions and clusters, or photosensitizing titania with organic dyes, which are often efficient but unstable.[6,7]

TiO_2 doped with C, N, or B has brought new perspectives because it renders the TiO_2 responsive to visible-light irradiation.[8] Investigations on alternative materials like bismuth are rare, although a number of reports have recently appeared concerning Bi-doped TiO_2 with high photocatalytic activities under visible-light irradiation.[9,10] Bian et al. reported the synthesis of an active Bi_2O_3/TiO_2 visible photocatalyst with an ordered mesoporous structure.[11] Wang et al. prepared bismuth- and sulfur-codoped TiO_2 by a simple sol–gel method; its high photocatalytic performance is associated with the existence of numerous oxygen vacancies, the acidic sites on the surface of TiO_2, and its high specific surface area.[12] Rengaraj and co-workers synthesized a Bi-doped TiO_2 nanocatalyst, and their degradation experiments demonstrated that the presence of Bi^{3+} in the TiO_2 catalysts substantially enhanced the photocatalytic degradation of methyl parathion under UV light.[13] However, the synthesis of highly ordered mesoporous Bi-doped TiO_2 has never been reported before.

Bi-doped TiO_2 photocatalysts have also been found to be active for the photodegradation of pollutants in aqueous solution.[14–19] Yao et al.[20,21] and Thanabodeekij et al.[22] reported that bismuth titanate compounds $Bi_xTi_yO_z$ were catalytically active for the photodecolorization of methyl orange

[a] S. Sajjad, S. A. K. Leghari, Dr. F. Chen, Prof. Dr. J. Zhang
Key Laboratory for Advanced Materials and
Institute of Fine Chemicals
East China University of Science and Technology
130 Meilong Road, Shanghai 200237 (P.R. China)
Fax: (+86) 21-64252062.
E-mail: jlzhang@ecust.edu.cn

[b] Prof. Dr. J. Zhang
School of Chemistry and Materials Science
Guizhou Normal University, Guiyang 550001 (P.R. China)

and photodegradation of 4-nitrophenol. They found that the Bi–O polyhedra in bismuth titanate compounds were photocatalytic centers. It was also suggested that the Bi^{3+} species in doped TiO_2 photocatalysts are active centers in the photoinduced degradation, reduction, or decolorization of pollutants.[9–11,13,14–19] Herein, we report simultaneous phenol oxidation and chromium reduction under visible irradiation by a Bi-modified mesoporous TiO_2.

Hexavalent chromium (chromium(VI)) is found together with a variety of aromatic compounds in a number of contaminated sites.[23,24] Organic pollutants, including phenol, naphthalene, and trichloroethylene, have been found at high concentrations in water containing chromium(VI).[25] Environments contaminated by chromium(VI) and its aromatic copollutants include groundwater aquifers, lakes, river sediments, and soils.[26] Chromium(VI) and its organic copollutants often originate from industrial sources such as leather tanning, photographic-film making, wood preservation, car manufacturing, petroleum refining, and agricultural activity. Chromium(VI) is a potent mutagen and a USEPA-classified group-A carcinogen because of its chronic and subchronic effects. On the other hand, the trivalent form of chromium(III) is about 1000 times less toxic than chromium(VI).[26] Xie et al. reported the simultaneous photocatalytic reduction of chromium(VI) and oxidation of phenol over monoclinic $BiVO_4$ under visible-light irradiation.[27] Wang et al. studied the photocatalytic reduction of chromium(VI) over various TiO_2 photocatalysts and the effects of dissolved organic species in UV light.[28]

Herein, we report the controllable and reproducible synthesis of a Bi-doped ordered mesoporous TiO_2 (ms-TiO_2), with variable Bi ratios from 0 to 4 mol% based on an ethanolic evaporation-induced self-assembly (EISA) process. Titanium isopropoxide (TIPO) and bismuth nitrate were used as precursors, with amphiphilic triblock copolymer (P123) as a template. We found that Bi species exist in various forms in the doped samples, and that the suitable doping of Bi significantly enhanced the photoactivity. The Bi-doped ordered mesoporous TiO_2 exhibits higher photocatalytic activities for the simultaneous oxidation of phenol and reduction of chromium in aqueous suspension than commercial photocatalyst P25 (Degussa P25) and Bi-doped conventional titania (Bi-doped conv-TiO_2). The promoting effects on the activity, mesoporosity, crystallinity and the modifying role of Bi species on the surface microstructure are investigated and discussed herein.

Results and Discussion

We have successfully synthesized a highly ordered hexagonal mesoporous Bi-doped TiO_2 with variable ratios through an ethanolic EISA process by using TIPO as a titania source and P123 as a template. Mesostructured Bi-doped TiO_2 samples undergo a self-assembly process of titanate oligomers hydrolyzed from TIPO and P123. The final nanocomposites have a uniform and homogeneous framework with doped Bi, as represented in Scheme 1. In this method, a high concentration of HCl simultaneously lowers the condensation and polymerization rates of TIPO, which renders it a controllable and reproducible method for producing highly ordered composite mesostructures.

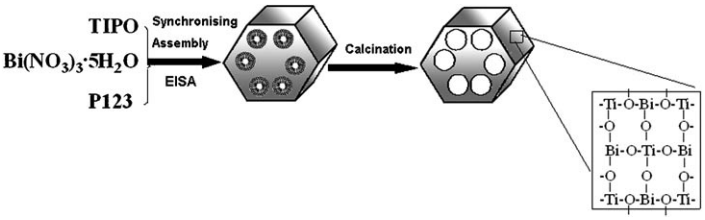

Scheme 1. Proposed mechanism of formation of ordered mesoporous TiO_2 with Bi doping.

The small-angle XRD (SAXRD) patterns of pure ms-TiO_2 and Bi-doped ms-TiO_2 with various levels of doping calcined at 350 °C are shown in Figure 1. All patterns show

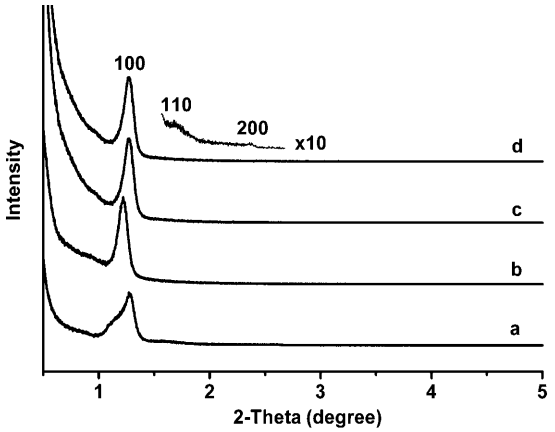

Figure 1. SAXRD of samples calcined at 350 °C: a) pure ms-TiO_2; b) 1.0% Bi-doped ms-TiO_2; c) 2.0% Bi-doped ms-TiO_2; d) 4.0% Bi-doped ms-TiO_2.

three well-resolved diffraction peaks of typical 2D hexagonal mesostructure with d-spacing ratios of $1:\sqrt{3}:2$, which are indexed as the 100, 110, and 200 reflections, respectively.[29–32] This indicates the highly stable, ordered 2D hexagonal mesostructure. Figure 2 shows the SAXRD patterns of 2.0% Bi-doped ms-TiO_2 calcined at three different temperatures. The principle diffractional peak (100) is clearly observed even after calcination at 400 °C, which shows relatively good thermal stability of the mesoporous structure. Increasing the calcination temperature results in a gradual decrease of diffractional strength due to the decrease in the degree of ordering of the mesoporous structure. The peak of calcined sample is shifted to lower angle, which corresponds to the increase in d-spacing due to pore-wall compacting, as well as to some smaller pores within the pore wall reorganizing to give larger pores. This implies that mesopores en-

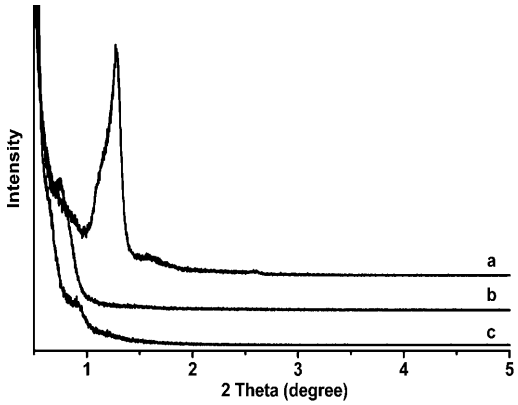

Figure 2. SAXRD of 2.0% Bi-doped ms-TiO_2 calcined at a) 350°C; b) 400°C; c) 450°C.

large as the calcination temperature increases. Further increase of the calcination temperature to 450°C corresponds to the weak appearance of the diffractional peak due to the collapse of the mesoporous structure and loss of long-range order. When the temperature reaches 500°C, no diffraction peak can be seen, which is due to the growth and coarsening of the anatase nanocrystallites.[33]

The wide-angle XRD (WAXRD) patterns of pure ms-TiO_2 and ms-TiO_2 with various levels of Bi-doped samples calcined at 350°C are shown in Figure 3. The pure ms-TiO_2

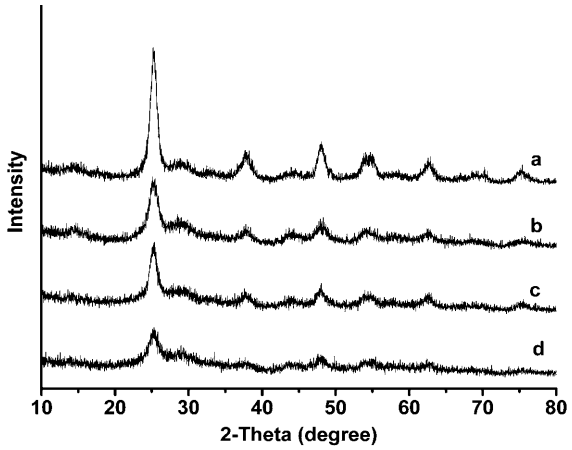

Figure 3. WAXRD of samples calcined at 350°C: a) pure ms-TiO_2; b) 1.0% Bi-doped ms-TiO_2; c) 2.0% Bi-doped ms-TiO_2; d) 4.0% Bi-doped ms-TiO_2.

and Bi-doped ms-TiO_2 samples display crystallized anatase phase, which corresponds to the characteristic diffractional peaks.[29,32,33] No significant diffractional peaks characteristic of the Bi phase are observed in the Bi-doped ms-TiO_2 samples. Clearly, the doping of Bi has not affected the crystal structure of photocatalysts, because of the extremely high dispersion and the lower content of Bi. With an increase in the Bi/TiO_2 ratio, the intensities of the diffraction peaks decrease, which indicates a decrease in the crystallinity of the anatase nanocrystals. The average particle size of the crystals is estimated from the widths of anatase (101) reflection by the Scherrer formula. The crystallization degree could be enhanced slightly with a further increase in calcination temperature (see Figure 4). The size of the pure and variously doped ms-TiO_2 nanocrystals in the framework matrix are calculated to be in the range of 7.2–6.3 nm.

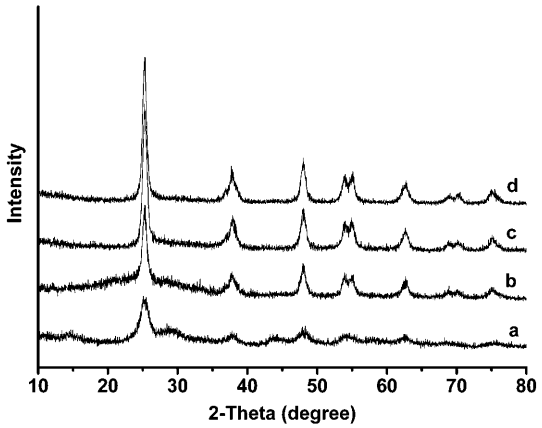

Figure 4. WAXRD of 2.0% Bi-doped ms-TiO_2 calcined at a) 350°C; b) 400°C; c) 450°C; d) 500°C.

Figure 5 shows the UV/Vis diffuse reflectance spectra (DRS) of the pure and variously doped ms-TiO_2 samples. The pure ms-TiO_2 is dominated by the edge relative to the O^{2-}–Ti^{4+} charge transition at 300–380 nm of TiO_2 anatase, which agrees well with previously reported results.[34,35] Pure mesoporous TiO_2 displays no significant absorbance in visible light due to its large bandgap of TiO_2 (3.2 eV). The Bi-doped ms-TiO_2 calcined at 350°C shows a spectral response in the visible region (400–700 nm) and the absorbance becomes stronger with increasing Bi content from 1.0 to 2.0%. A change of color from white to brownish yellow is observed from 0 to 2.0%. Briefly, the Bi_2O_3 photosensitizer

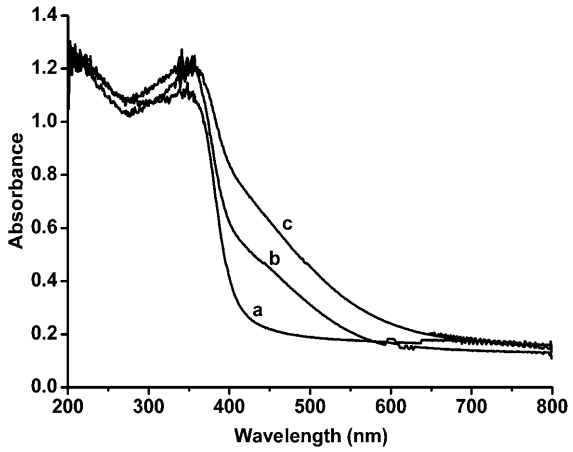

Figure 5. UV/Vis diffuse reflectance spectra of samples calcined at 350°C: a) pure ms-TiO_2; b) 1.0% Bi-doped ms-TiO_2; c) 2.0% Bi-doped ms-TiO_2.

with narrow energy gap (2.8 eV) can be easily activated by visible light and induced photoelectrons and holes. In the absence of TiO_2, these electrons and holes may recombine rapidly owing to the narrow energy gap, which leads to the quenching of the spectral response. In Bi-doped ms-TiO_2, the recombination between photoelectrons and holes can be effectively inhibited, which leads to a strong response in the visible range.[36] This wide visible-light response mainly originates from the formation of surface-defect centers, which are associated with existence of oxygen vacancies created by the doping process. Consequently, 2.0% Bi-doped ms-TiO_2 reduces the energy gap of the catalyst, thereby shifting the excitation source from UV to the visible light.

Figure 6 shows the Raman spectra of pure ms-TiO_2 and ms-TiO_2 with various levels of Bi doping. The Raman bands

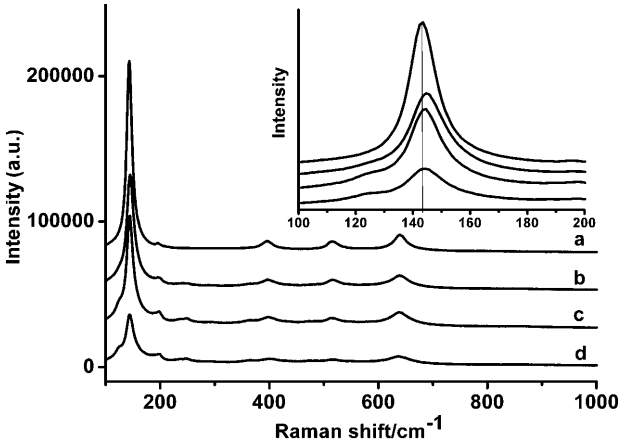

Figure 6. Raman spectra of a) pure ms-TiO_2; b) 1.0% Bi-doped ms-TiO_2; c) 2.0% Bi-doped ms-TiO_2; d) 4.0% Bi-doped ms-TiO_2.

of TiO_2 appear at 146.3, 196.3, 397.3, 517.6, and 638.7 cm^{-1}. The bands typical of anatase can be seen at 146.0, 196.0, 397.0, 516.0, and 638.0 cm^{-1},[37] and can be assigned to the E_g, B_{1g}, A_{1g}, B_{2g}, and E_g vibrational modes of TiO_2, respectively. These results are consistent with the XRD measurements. The absorption at 146 cm^{-1} indicates an anatase crystalline framework structure.[38] The absorption becomes broader and weaker, and shifts positively by 4 cm^{-1} when the Bi content increases from 1.0 to 2.0%, which suggests increased crystalline defects within the framework.[38] Such defects may favor the capture of photoelectrons and thus inhibit charge recombination. Meanwhile, Bi-doped nanoparticles on the surface framework may also serve as electron conductors, which facilitates photoelectron transfer to the pore surface, and further reduces the probability of charge recombination. When the Bi content is further increased from 2.0 to 4.0%, no significant effect on the Raman peak position is observed.

Photoluminescence (PL) emission spectra have been widely used to investigate the change of surface states of TiO_2, the efficiency of charge-carrier trapping, migration, and transfer to understand the fate of electron–hole pairs in semiconductor particles.[39] Figure 7 shows room temperature photoluminescence spectra for pure ms-TiO_2 and ms-TiO_2 with various levels of Bi doping. In this study, the PL

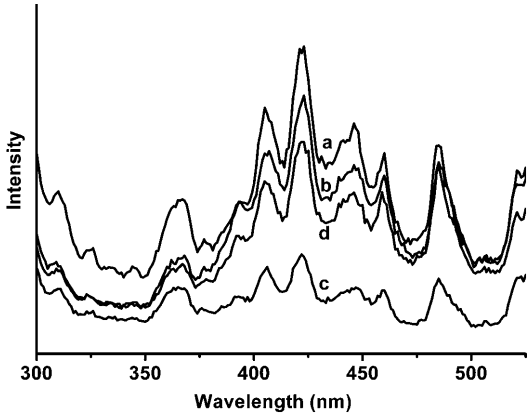

Figure 7. PL emission spectra of a) pure ms-TiO_2; b) 1.0% Bi-doped ms-TiO_2; c) 2.0% Bi-doped ms-TiO_2; d) 4.0% Bi-doped ms-TiO_2.

spectra of all samples were examined in the range of 300–550 nm. The PL spectrum of the pure ms-TiO_2 is higher in intensity than the spectra of the Bi-doped ms-TiO_2 samples. The PL intensity greatly decreases with the increased presence of bismuth. As for the pure ms-TiO_2, well-resolved peaks at 365, 405, 424, 451, 461, 486, and 528 nm were observed. All these peaks can be ascribed to surface traps.[40,41] The excitonic PL intensity of the Bi-doped ms-TiO_2 samples decreases as the Bi content increases up to 2.0%. It then increases again with an increase in Bi content up to 4.0%. It can be clearly observed from Figure 7 that Bi-doped TiO_2 shows a decrease in PL intensity compared to the blank ms-TiO_2, which reflects the decrease in trap states on the surface of TiO_2. This indicates that TiO_2 incorporated with an appropriate amount of Bi may slow the radiative recombination process of photogenerated electrons and holes in TiO_2. The slower recombination of the photogenerated charges is advantageous for photocatalysis. The observed PL spectra are attributed to the radioactive recombination of either self-trapped excitons[42] or hydroxylated Ti^{3+} surface complexes[43] from the charge-transfer excited state of the highly dispersed TiO_2 species. The reduction in PL intensity indicates a decrease in radioactive recombination processes. These experimental results demonstrate that PL spectra are quite sensitive to the level of Bi doping. When the Bi content is lower than its optimal ratio, the Bi impurity energy level would be a separation center and reduce the electron–hole recombination. On the contrary, when the content of Bi was higher than its optimal ratio, the Bi impurity energy level would be a recombination center.

Transmission electron microscopy (TEM) images (see Figure 8) viewed along the [001] and [110] directions confirm that Bi-doped ms-TiO_2 products calcined at 350°C have a highly ordered 2D hexagonal regularity. The TEM images (Figure 8a and b) show that the 2.0% Bi-doped ms-TiO_2 cal-

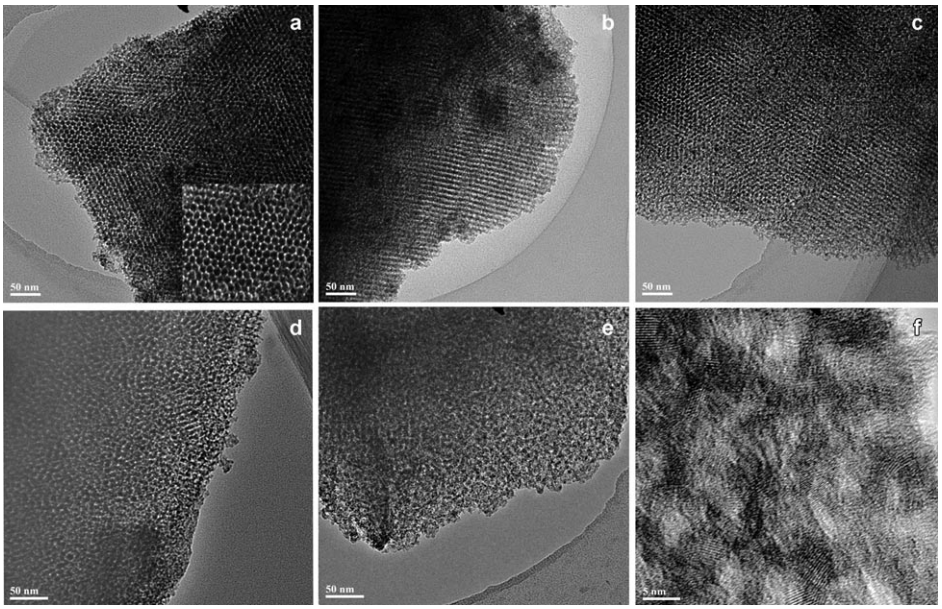

Figure 8. a,b) TEM images of 2.0% Bi-doped ms-TiO_2 calcined at 350°C; c) 4.0% Bi-doped ms-TiO_2 calcined at 350°C; d) 2.0% Bi-doped ms-TiO_2 calcined at 400°C; e) 2.0% Bi-doped ms-TiO_2 calcined at 450°C; f) HRTEM of 2.0% Bi-doped ms-TiO_2 calcined at 400°C.

cined at 350°C displays highly ordered mesoporous channels with average diameter of 6.5 nm. No significant Bi particles are observed in the pore channels or on the outer surface, which implies the extremely high dispersion of the particles.[11] The size of the anatase nanocrystals evaluated from the TEM images is about 6.6 nm. This is consistent with the results calculated from WAXRD patterns. The average pore-wall thickness is about 3.8 nm. The increase of Bi content in the Bi-doped ms-TiO_2 had no considerable effect on the mesoporous structure. The Bi particles do not appear in the pore channels, or even on the outer surface of the 4.0% Bi-doped ms-TiO_2 (Figure 8c), due to the lower content of Bi. Figure 8d demonstrates that calcination of the 2.0% Bi-doped ms-TiO_2 at 400°C partially damages the mesoporous structure. As shown in Figure 8e, the mesoporous structure is destroyed after calcination at 450°C, which is in accordance with the results from low-angle XRD patterns. The high-resolution TEM (HRTEM) image of 2.0% Bi-doped ms-TiO_2 at 400°C (Figure 8f) shows that the average d-spacing of the lattice fringes measured from the TEM images is about 0.34 nm, which agrees well with the d 101 value of 0.35 nm calculated from the corresponding WAXRD patterns. Such pore walls are composed of highly crystallized anatase.[44]

N_2 adsorption–desorption isotherms of 2D hexagonal Bi-doped ms-TiO_2 samples calcined at 350°C with 0 to 4.0 mol% Bi are displayed in Figure 9. The isotherms exhibit typical type IV curves with a sharp capillary condensation step at relative pressure (P/P_o) of 0.7, which suggests a narrow pore-size distribution. The hysteresis loop is very close to being H_1 type, which implies uniform cylindrical pore geometry.[32,45] The attached pore-size distribution demonstrates a narrow pore-diameter range. The surface area, pore volume, and pore diameter are calculated from the N_2 adsorption–desorption isotherms. Table 1 shows that the undoped ms-TiO_2 and Bi-doped ms-TiO_2 samples obtained through the EISA method exhibit much higher surface areas than both Degussa P-25 and Bi-doped conv-TiO_2 prepared by the conventional sol–gel method. The pore size calculated from the adsorption data using the Barret–Joyner–Halenda (BJH) model are in the range of 6.0–7.3 nm (inset Figure 9). The calculated BET specific surface areas are in the range of 207–157 $m^2 g^{-1}$. For the Bi-doped ms-TiO_2 samples, both surface area and pore volume decrease while the pore diameter increases with higher

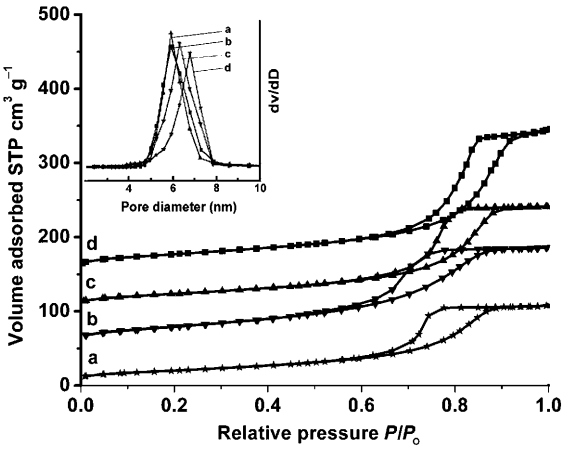

Figure 9. N_2 sorption data of a) pure ms-TiO_2; b) 1.0% Bi-doped ms-TiO_2; c) 2.0% Bi-doped ms-TiO_2; d) 4.0% Bi-doped ms-TiO_2.

Table 1. BET surface areas and pore properties of pure ms-TiO_2 and the various Bi-doped composites.

Sample	S_{BET} $[m^2 g^{-1}]$[a]	Pore volume $[cm^3 g^{-1}]$[b]	Pore size [nm][c]
pure ms-TiO_2	207	0.25	6.0
1.0% Bi-doped ms-TiO_2	191	0.25	6.2
2.0% Bi-doped ms-TiO_2	180	0.24	6.5
4.0% Bi-doped ms-TiO_2	157	0.23	7.3
2.0% Bi-doped conv-TiO_2	55	–	–

[a] BET surface area calculated from the linear part of the BET plot. [b] Estimated by the BJH method. [c] Estimated by using the desorption branch of the isotherm.

Bi content, which is due to the intrusion of Bi particles in the pore channels of TiO_2 structure. However, the bismuth content up to 4.0% low enough to be detected by XRD and TEM analyses.

Quantitative XPS analysis was performed on powders of pure ms-TiO_2 and ms-TiO_2 with various levels of Bi doping, as shown in figure 10, which shows the high-resolution spectra for the Ti2p, O1s and Bi 4f regions for the samples. All samples contain only Ti, O, Bi, and C. The C can be ascribed to adventitious hydrocarbon from the XPS instrument itself. The XPS spectra of the Bi 4f region of the Bi-doped ms-TiO_2 are given in Figure 10A. To determine the oxidation state of the bismuth dopant, the binding energies of Bi $4f_{7/2}$ and Bi $4f_{5/2}$ for pure Bi_2O_3 at 158.6 and 163.9 eV, respectively, were taken from previous reports and accepted as standard for the XPS measurement.[46–48] Figure 10A shows that with the increasing Bi content, the intensity of the Bi 4f peaks increases and the binding energies of the Bi 4f peaks shift toward higher values. The binding energies of Bi $4f_{7/2}$ and Bi $4f_{5/2}$ are increased to 158.9 and 164.2 eV, respectively, which are higher than the values of pure Bi_2O_3. The positive shift is attributed to $Bi^{(3+x+)}$ state.[48] It indicates a strong interaction between Bi and TiO_2, and that the Bi^{3+} centers are partially oxidized to $Bi^{(3+x+)}$. The ionic radii of the more oxidized forms of Bi are smaller than that of Bi^{3+} (1.17 Å).[49] This enhancement of binding energy may be due to the formation of Bi–O–Ti bonds in the framework of titania. These results are consistent with the Raman measurements.

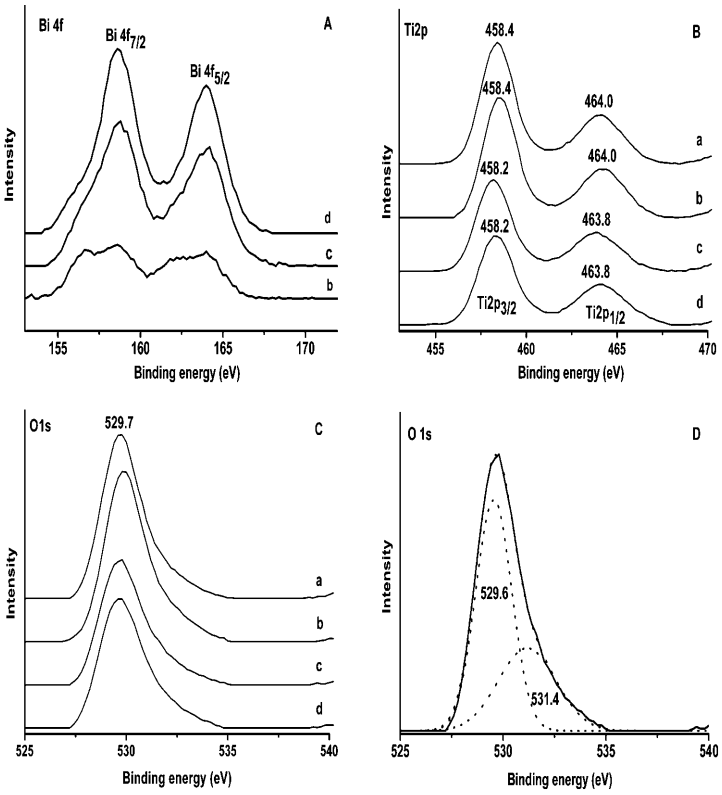

Figure 10. High-resolution XPS spectra of A) Bi 4f; B) Ti 2p; C) O 1s regions; D) O 1s region in curve fit data of 2.0% Bi-doped ms-TiO_2; a) pure ms-TiO_2; b) 1.0% Bi-doped ms-TiO_2; c) 2.0% Bi-doped ms-TiO_2; d) 4.0% Bi-doped ms-TiO_2.

Figure 10B shows that the Ti 2p orbital splits into two peaks $2p_{1/2}$ and $2p_{3/2}$. The Ti $2p_{1/2}$ and Ti $2p_{3/2}$ spin–orbital splitting photoelectrons for the sample are located at binding energies of about 464.2 and 458.4 eV, respectively, which is in agreement with previously reported values.[41–44] There is a slight decrease in the binding energy of Ti 2p in the 2.0 and 4.0% Bi samples, as indicated in Figure 10B. The slight decrease in binding energy of Ti 2p suggests that some Ti^{4+} ions are converted to a lower oxidation state, such as Ti^{3+}.[10] Therefore, it illustrates that the Ti oxidation state is lowered with Bi substitutions.[17,50] On the other hand, the O1s region also shows a slight decrease in binding energy as shown in Figure 10C. In 2.0% Bi-doped ms-TiO_2, the O1s region shows two peaks, as can be seen in Figure 10D. The first peak is located at 529.6 eV, which is assigned to Ti–O in TiO_2, whereas the second peak, at 531.4 eV, is ascribed to the oxygen attached to bismuth (Bi–O bond).[35] It has been suggested that the second peak is associated with hydroxyl groups.[51] The XPS and Raman results infer that the Bi–O–Ti bonds were formed in the Bi-doped ms-TiO_2 samples. The Bi/Ti molar ratios of the various bismuth-doped ms-TiO_2 samples calculated by XPS data are 0.018, 0.056, and 0.134 for the 1.0, 2.0, and 4.0% samples, respectively.

The simultaneous photocatalytic oxidation of phenol and chromium(VI) reduction were employed to evaluate the photocatalytic activities of pure ms-TiO_2 and the Bi-doped ms-TiO_2 samples. No detectable degradation of phenol and chromium is observed without catalyst. After 150 min of irradiation, 95% oxidation of phenol and 90% of chromium reduction are observed. Figure 11a shows the comparison of oxidation of phenol and reduction of chromium after 150 min in visible light with the various Bi-doped ms-TiO_2 samples, pure ms-TiO_2, Degussa P25, and Bi-doped conv-TiO_2. Modification of ms-TiO_2 with 2.0% Bi-doped ms-TiO_2 results in an abrupt increase of the photocatalytic activity relative to pure Degussa P25 and 2.0% Bi-doped conv-TiO_2. The absorption of 2.0% Bi-doped ms-TiO_2 is more redshifted, and reduces the electron–hole recombination more efficiently. This wide visible-light response mainly originates from the existence of oxygen vacancies created by the doping process. Consequently, there is an optimum concentration of loaded ions, at which the thickness of the space–charge layer is approximately equal to the light-penetration depth. As the concentration of dopant ions increases towards the optimum amount, the surface barrier increases, and the space–charge region becomes narrower. The electron–hole pairs within the region are efficiently separated before recombination. In the case of Bi-doped ms-TiO_2, the photoinduced hole centers are formed as a result of the photogenerated electrons trapped by the pre-existing oxygen vacancies under visible light.[52,53] Bi introduced into the anatase titania acts as an electron acceptor, which aids the ef-

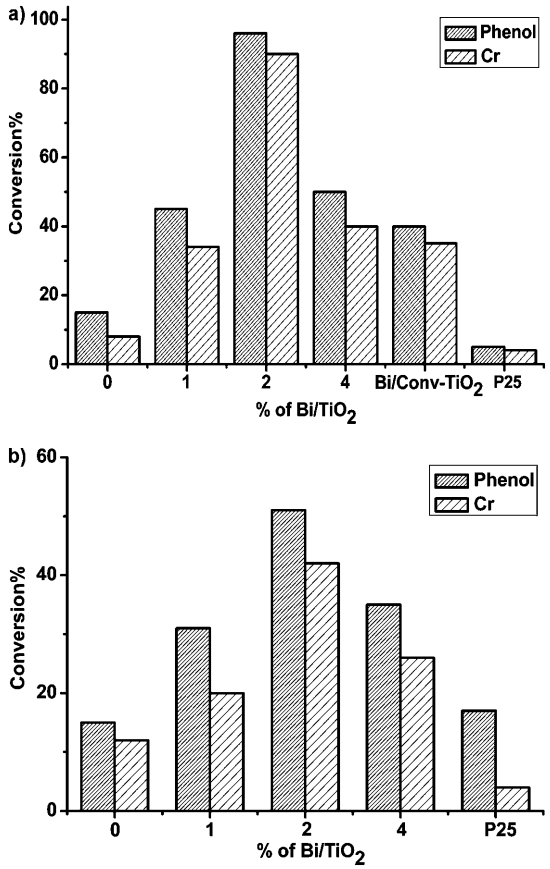

Figure 11. Phenol oxidation and chromium reduction profiles over pure ms-TiO_2, the various Bi-doped ms-TiO_2, 2% Bi-doped conv-TiO_2 samples, and P25 under a) visible and b) UV irradiation.

fective separation of electron–hole pairs photogenerated in the TiO_2, and inhibits their recombination. The higher activity of Bi-doped ms-TiO_2 is also attributed to its higher surface area, which can enhance light harvesting and adsorption for reactant molecules. The mesopores are beneficial for photocatalysis, since more accessible active sites are available for the photocatalytic process. Moreover, better connectivity of mesopores provides more pathways for the reactants to enter and for products to escape from the network. These mesoporous characteristics are crucial to photocatalytic reactions, especially for degrading large molecular pollutants.

All the Bi-doped ms-TiO_2 samples show higher activity than pure ms-TiO_2 and Degussa P25 under UV irradiation, as shown in Figure 11b. This indicates that the existence of Bi is favorable for the separation of photogenerated electron–hole pairs, and it also directly confirms the PL results.

The photocatalytic efficiency of pure ms-TiO_2 and the various Bi-doped ms-TiO_2 samples are also evaluated for a single pollutant system; for either phenol oxidation or chromium reduction. The 2.0% Bi-doped ms-TiO_2 sample gave 58% phenol oxidation and 54% chromium reduction for the single systems. The 2.0% Bi-doped ms-TiO_2 sample exhibits the best activity of all the composites and P25 under visible light, as shown in Figure 12.

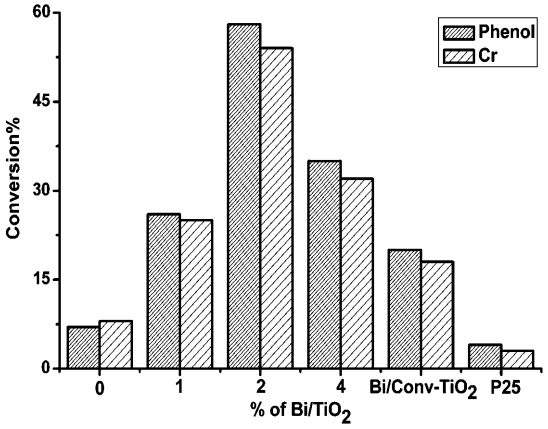

Figure 12. Phenol oxidation and chromium reduction profiles for the single pollutant systems over pure ms-TiO_2, the various Bi-doped ms-TiO_2 samples, 2% Bi-doped conv-TiO_2, and P25 under visible light.

To determine the effect of calcination temperature on photocatalytic activity, the 2.0% Bi-doped ms-TiO_2 sample calcined at various temperatures was employed for simultaneous phenol oxidation and chromium reduction. The sample calcined at 350°C showed the highest activity. Calcination at higher temperature, as shown in Figure 13, caused a decrease in activity, which was mainly attributed to the damage of long-range order in the mesoporous structure, as indicated by the TEM results.

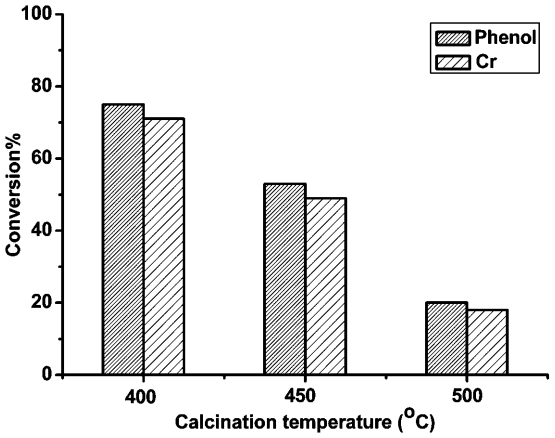

Figure 13. Phenol oxidation and chromium reduction profiles over 2.0% Bi-doped ms-TiO_2 calcined at three different calcination temperatures.

In traditional noble-metal/titania composites, such as Pt/TiO_2 and Au/TiO_2, the noble metals have been demonstrated to serve as trapping centers for electrons generated in light-activated TiO_2, thereby leading to improved quantum efficiency. The role of Bi is similar to the noble metal in this system. The incorporation of Bi induces the formation of Bi^{3+} and $Bi^{(3+x+)}$ species, which act as trapping sites for the electrons, and thus benefit the separation of the electron–hole pairs. Generally, the photocatalytic activity of a catalyst

for the photooxidation of organic compounds is mainly related to the position of the valence band of the photocatalyst and the mobility of the photogenerated carriers.[54,55] In the hybridized valence band of Bi-doped TiO_2, the photogenerated holes show high mobility, which contributes to the high activity of the photocatalyst. However, very high Bi content (>2.0%) is harmful for the photoactivity. Because the high Bi content, rather than facilitating charge transport and reducing charge recombination, may lead to the Bi species acting as centers of electron–hole recombination, which would reduce quantum efficiency,[49,56] as confirmed in our PL study. It was found that the 2.0% Bi-doped ms-TiO_2 obtained through the EISA method exhibited much higher activity than the 2.0% Bi-doped conv-TiO_2 prepared by conventional sol–gel method.

The photo-reduction of chromium(VI) to chromium(III) and the oxidation of phenol can be achieved through a photocatalytic process by using a novel visible-light active Bi-doped ms-TiO_2 catalyst, with the mechanism as shown in Scheme 2. From the results of XPS, we found that the addition of Bi creates Bi^{3+} and $Bi^{(3+x+)}$ species. The redox potential E^o ($Bi^{(3+x+)}/Bi^{3+}$) = −0.29 V lies between the conduction-band potential of TiO_2 (E_{cb} = −0.5 V versus normal hydrogen electrode (NHE)) and the valence-band potential (E_{vb} = 2.7 V versus NHE). By comparing the PL and UV/Vis spectra, we found that the photogenerated electron–hole pairs are effectively separated under the visible irradiation. In other words, this range of light contributes to the catalytic degradation of phenol and chromium(VI) reduction. Therefore, we conclude that the degradation of pollutants must depend on the separation of the electron–hole pairs of the catalyst generated by the visible-light. The experimental results also support the above inference. In Bi-doped ms-TiO_2, the bismuth doping creates the energy level below the conduction band of TiO_2, which results in a reduction of band-gap energy, as shown in Scheme 2. Visible irradiation of Bi-doped ms-TiO_2 produces electron–hole pairs [Eq. (1)] at the surface of the photocatalyst; the electrons are trapped by the $Bi^{(3+x+)}$, which is converted to Bi^{3+} species, and this aids the separation of the electron–hole pairs:

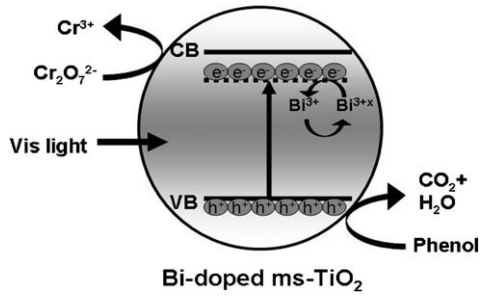

Scheme 2. Proposed mechanism of phenol oxidation and chromium reduction on Bi-doped ordered ms-TiO_2 photocatalyst.

$$TiO_2 + Bi^{(3+x+)} + vis(h\nu) \rightarrow TiO_2(h^+) + Bi^{(3+)}(e^-) \quad (1)$$

After electron–hole separation, the electrons can be scavenged by chromium(VI), which in turn is reduced to chromium(III) [Eq. (2)]. The holes can then produce OH radicals [Eq. (3)], which can further degrade the phenol to CO_2 and H_2O [Eq. (4)]. Of course, the holes can also directly oxidize the organic molecules [Eq. (5)]:

$$Cr_2O_7^{2-} + 14H^+ + 6e^- \rightarrow 2Cr^{3+} + 7H_2O \quad (2)$$

$$H_2O + h^+ \rightarrow {}^{\bullet}OH + H^+ \quad (3)$$

$${}^{\bullet}OH + \text{phenol} \rightarrow CO_2 + H_2O \quad (4)$$

$$h^+ + \text{phenol} \rightarrow CO_2 + H_2O \quad (5)$$

In the presence of organic species, the photogenerated holes are rapidly scavenged from the Bi-doped ms-TiO_2 particles, which suppress electron–hole recombination on the catalyst surface and accelerate the reduction of chromium(VI) by photogenerated electrons.[57] One of the important strategies of promoting the photocatalytic reduction of chromium(VI) is to enhance the charge separation which can be achieved by improving the structure of the photocatalyst, and by introducing scavengers of holes and/or electrons in the solution. It has been reported that the presence of organic species as sacrificial electron donors can accelerate the photocatalytic reduction of chromium(VI).[58,59]

Theoretically, in the photoelectrochemical process the number of charges involved in reduction by conduction-band electrons and oxidation by valence-band holes must be equal. Thus, one can expect that the promoting effect of both pollutants is mutual; in other words, the presence of phenol enhances the reduction of chromium(VI) to chromium(III). This mutual promoting effect provides an important support for Bi-doped ms-TiO_2 as a visible-light catalyst for efficient simultaneous removal of phenol and chromium(VI) by photocatalytic oxidation and reduction, respectively, in the same system.

Conclusion

The highly ordered 2D hexagonal mesoporous Bi-doped ms-TiO_2 composites with variable Bi ratios have been successfully synthesized by using a synchronous assembly approach based on the ethanolic EISA process. The highly ordered mesoporous Bi-doped TiO_2 with 2D hexagonal structure can be obtained by adding a large amount of HCl under low relative humidity and evaporation temperature. Ordered mesoporous Bi-doped ms-TiO_2 contained crystalline anatase which was uniformly embedded in the pore walls. Bi-doped ms-TiO_2 samples showed an extension of light absorption into the visible region, which mainly originates from the doping process with the formation of new states of Bi in the form of Bi–O–Ti bonds and reduction of the electron–hole recombination rate. The Bi-doped ms-TiO_2 samples exhibited improved photocatalytic activities over the commercial

catalyst P25 and Bi-doped conv-TiO_2 in the simultaneous degradation of phenol and reduction of chromium in aqueous suspension under visible and UV irradiation.

Experimental Section

Materials: Titanium isopropoxide ([Ti{OCH(CH_3)$_2$}$_4$], TIPO), bismuth nitrate ($Bi(NO_3)_3{\cdot}5H_2O$), ethanol (absolute), and concentrated HCl (36.5wt%) were AR grade. Pluronic P123 [(M_w) 5800, HO-($CH_2CH_2O)_{20}$(CH_2-$CHCH_3O)_{70}$($CH_2CH_2O)_{20}$H, $EO_{20}PO_{70}EO_{20}$, abbreviated as P123], was purchased from Aldrich. All the above chemicals were purchased from Shanghai Sinopharm Chemical Reagent Co. P25 (a commercial nanocrystalline TiO_2 that consists of ca. 80% anatase and 20% rutile; BET area ca. 50.0 m^2g^{-1}) was supplied by Degussa. All the chemicals were used as received without further purification. Double-distilled water was used throughout the experiments.

Catalyst preparation: For a typical synthesis, copolymer P123 (1.0 g) was dissolved in ethanol (30.0 g), and then concentrated HCl (1.8 g) was slowly added with vigorous stirring. After heating in a sealed bottle at 40 °C for 3 h, TIPO (3.0 g) and $Bi(NO_3)_3{\cdot}5H_2O$ were added and the reaction was stirred vigorously for 5 h at 40 °C. The resulting sols were sonicated for 30 min before being transferred into Petri dishes and evaporated at 35 °C in air with relative humidity of 50–60% for about four days to produce transparent membranes, which were then dried at 80 °C for six days. The samples were calcined at 350 °C for 4 h in air to remove organic templates. Samples containing 1.0, 2.0, and 4.0 mol% Bi were prepared and subsequently calcined at various temperatures for 2 h in air. For comparison, pure mesoporous TiO_2 was also prepared by the same method without the addition of dopant. The samples were denoted as x% Bi-doped ms-TiO_2, where x% refers to the Bi molar ratio. For comparison, the Bi-doped TiO_2 samples were also prepared by using the traditional sol–gel method without adding P123. These samples were designated as x% Bi-doped conv-TiO_2.

Characterization: XRD patterns for all samples were collected in the range 20–80° (2θ) for WAXRD and 0.5–8° (2θ) for SAXRD with a Rigaku D/MAX 2550 diffractometer ($Cu_{K\alpha}$ radiation, $\lambda = 1.5406$ Å), operated at 40 kV and 100–200 mA. The crystallite size was estimated by applying the Scherrer equation to the full width at half-maximum (fwhm) of the (101) peak of anatase. $D = k\lambda/\beta\cos\theta$, where β is the half-height width of the diffraction peak of anatase, $K = 0.89$ is a coefficient, θ is the diffraction angle, and λ is the X-ray wavelength corresponding to $Cu_{K\alpha}$ irradiation. The UV/Vis absorbance spectra were obtained for the dry-pressed disk samples using a Scan UV/Vis spectrophotometer (Varian, Cary 500) equipped with an integrating sphere assembly, with $BaSO_4$ as the reflectance sample. The spectra were recorded at room temperature in air within the range 200–800 nm. Raman spectra of the samples were recorded with a Renishaw inVia Raman spectrometer at room temperature with excitation wavelength 785 nm. The morphologies were observed by using TEM (TEM, JEOL JEM2010). PL spectra were recorded with a Varian Cary Eclipse Fluorescence spectrophotometer with excitation at 270 nm. The instrument employed for XPS was a Perkin–Elmer PHI 5000C ESCA System with $Al_{K\alpha}$ radiation operated at 250 W. The shift of binding energy due to relative surface charging was corrected using the C 1s level at 284.6 e.V as an internal standard. Nitrogen adsorption and desorption isotherms were obtained at 77 K with a Micromeritics ASAP 2010 system. All the samples were degassed at 473 K before measurement.

The simultaneous chromium reduction and phenol oxidation were carried out in a 100 mL quartz photochemical reactor. The reaction solution contains 0.05 g catalyst mixed with 50 mL aqueous solution of 6.0×10^{-4} M phenol and 4.0×10^{-4} M $K_2Cr_2O_7$. A 1000 watt halogen lamp was used as the visible light source. The short-wavelength components ($\lambda < 420$ nm) of the light were removed using a cut-off glass filter. A 300 watt high-pressure Hg lamp with strongest emission wavelength of 365 nm was used as the UV light source. During the reaction, a water-cooling system maintained the photochemical reactor at room temperature. The distance between the lamp and the center of quartz tube was 10 cm. Prior to illumination, the suspension was sonicated for 10 min and then magnetically stirred in darkness for 30 min to establish adsorption–desorption equilibrium at room temperature. During irradiation, stirring was maintained to keep the mixture in suspension. The samples were centrifuged to separate the photocatalyst for analysis. The concentration and conversion of phenol and chromium(VI) were analyzed at their characteristic wavelengths (phenol = 270 nm, chromium(VI) = 350 nm) using a Cary100 UV/Vis spectrophotometer. Preliminary results indicated a linear relationship between light absorbance and phenol or chromium(VI) concentration, and showed that the decomposition of phenol or reduction of chromium(VI) in the absence of photocatalyst or irradiation was negligible. The reproducibility was checked by repeating the measurements at least three times, and was found to be within the acceptable limit (±3%).

Acknowledgements

This work has been supported by National Nature Science Foundation of China (20773039, 20977030), the National Basic Research Program of China (973 Program, 2007CB613301, 2010CB732306), the Science and Technology Commission of Shanghai Municipality (10520709900), and the Fundamental Research Funds for the Central Universities. S.S. and S.A.K.L. also thank the Higher Education Commission (Pakistan) for financial support.

[1] M. E. Davis, *Nature* **2002**, *417*, 813–821.
[2] S. Yuan, Q. Sheng, J. Zhang, F. Chen, M. Anpo, W. Dai, *Catal. Lett.* **2006**, *107*, 19–24.
[3] A. M. Liu, K. Hidajat, S. Kawi, D. Y. Zhao, *Chem. Commun.* **2000**, 1145–1146.
[4] J. C. Yu, X. C. Wang, W. Ho, *Adv. Funct. Mater.* **2004**, *14*, 1178–1183.
[5] R. Asahi, T. Morikawa, T. Ohwaki, Y. Taga, *Science* **2001**, *293*, 269–271.
[6] I. M. Arabatzis, T. Stergiopoulos, D. Andreeva, S. Kitova, S. G. Neophytides, P. Falaras, *J. Catal.* **2003**, *220*, 127–135.
[7] H. Hao, J. Zhang, *Microporous Mesoporous Mater.* **2009**, *121*, 52–57.
[8] S. In, A. Orlov, R. Berg, F. Garcia, S. Pedrosa-Jimenez, M. S. Tikhov, D. S. Wright, R. M. Lambert, *J. Am. Chem. Soc.* **2007**, *129*, 13790–13791.
[9] J. X. Yu, S. W. Liu, Z. L. Xiu, W. N. Yu, G. J. Feng, *J. Alloys Compd.* **2008**, *461*, L17–L19.
[10] W. J. Hong, M. Kang, *Mater. Lett.* **2006**, *60*, 1296–1305.
[11] Z. F. Bian, J. Zhu, S. H. Wang, Y. Cao, X. F. Qian, H. X. Li, *J. Phys. Chem. C* **2008**, *112*, 6258–6262.
[12] Y. Wang, Y. Wang, Y. Meng, H. M. Ding, Y. K. Shan, *J. Phys. Chem. C* **2008**, *112*, 6620–6626 .
[13] S. Rengaraj, X. Z. Li, P. A. Tanner, Z. F. Pan, G. K. H. Pang, *J. Mol. Catal. A* **2006**, *247*, 36–43.
[14] S. Rengaraj, X. Z. Li, *Chemosphere* **2007**, *66*, 930–938.
[15] J. Xin, S. Zhang, G. Qi, X. Zheng, W. Huang, S. Wu, *React. Kinet. Catal. Lett.* **2005**, *86*, 291–298.
[16] Y. Bessekhouad, D. Robert, J. V. Weber, *Catal. Today* **2005**, *101*, 315–321.
[17] M. Kang, Y. R. Ko, M. K. Jeon, S. C. Lee, S. J. Choung, J. Y. Park, S. Kim, S. H. Choi, *J. Photochem. Photobiol. A* **2005**, *173*, 128–136.
[18] J. J. Xu, Y. H. Ao, D. G. Fu, C. W. Yuan, *Appl. Surf. Sci.* **2008**, *255*, 2362–2365.
[19] H. S. Zuo, J. Sun, K. J. Deng, R. Su, F. Y. Wei, D. Y. Wang, *Chem. Eng. Technol.* **2007**, *30*, 577–582.
[20] W. F. Yao, H. Wang, X. H. Xu, X. F. Cheng, J. Huang, S. X. Shang, X. N. Yang, M. Wang, *Appl. Catal. A* **2003**, *243*, 185–190.
[21] W. F. Yao, X. H. Xu, H. Wang, J. T. Zhou, X. N. Yang, Y. Zhang, S. X. Shang, B. B. Huang, *Appl. Catal. B* **2004**, *52*, 109–116.

[22] N. Thanabodeekij, E. Gulari, S. Wongkasemjit, *Powder Technol.* **2005**, *160*, 203–208.
[23] A. Kouzeli-Katsiri, N. Kartsonas, A. Priftis, *Environ. Technol. Lett.* **1988**, *9*, 261–270.
[24] C. W. Kuo, B. R. S. Genthner, *Appl. Environ. Microbiol.* **1996**, *62*, 2317–2323.
[25] R. R. Patterson, S. Fendorf, M. Fendorf, *Environ. Sci. Technol.* **1997**, *31*, 2039–2041.
[26] S. Beszedits, *Chromium in the Natural and Human Environments*, (Eds.: O. Nriagu, E. Nieboer), Wiley, New York, **1988**, pp. 232–263.
[27] B. Xie, H. Zhang, P. Cai, R. Qiu, Y. Xiong, *Chemosphere* **2006**, *63*, 956–963.
[28] L. Wang, N. Wang, L. Zhu, H. Yu, H. Tang, *J. Hazard. Mater.* **2008**, *152*, 93–99.
[29] P. D. Yang, Y. Zhao, D. I. Margolese, B. F. Chmelka, G. D. Stucky, *Nature* **1998**, *396*, 152–155.
[30] B. Z. Tian, X. Y. Liu, B. Tu, C. Z. Yu, J. Fan, L. M. Wang, S. H. Xie, G. D. Stucky, D. Y. Zhao, *Nat. Mater.* **2003**, *2*, 159–163.
[31] S. Yuan, Q. Sheng, J. Zhang, F. Chen, M. Anpo, Q. Zhang, *Micropor. Mesopor. Mater.* **2005**, *79*, 93–99.
[32] S. Y. Choi, M. Mamak, N. Coombs, N. Chopra, G. A. Ozin, *Adv. Funct. Mater.* **2004**, *14*, 335–344.
[33] D. L. Li, H. S. Zhou, I. Honma, *Nat. Mater.* **2004**, *3*, 65–72.
[34] A. K. L. Sajjad, S. Shamaila, B. Tian, F. Chen, J. Zhang, *Appl. Catal. B* **2009**, *91*, 397–405.
[35] D. N. Ke, H. J. Liu, T. Y. Peng, X. Liu, K. Dai, *Mater. Lett.* **2008**, *62*, 447–450.
[36] Y. Wu, G. Lu, S. Li, *J. Phys. Chem. C* **2009**, *113*, 9950–9955.
[37] I. R. Beattie, T. R. Gilson, *J. Chem. Soc. A* **1969**, 2322–2327.
[38] J. C. Parker, R. W. Siegel, *Appl. Phys. Lett.* **1990**, *57*, 943–945.
[39] H. Yamashita, H. Y. Ichihashi, S. G. Zhang, Y. Matsumura, Y. Souma, T. Tatsumi, M. Anpo, *Appl. Surf. Sci.* **1997**, *121*, 305–309.
[40] T. Toyoda, T. Hayakawa, K. Abe, T. Shigenari, Q. Shen, *J. Lumin.* **2000**, *87–89*, 1237–1239.
[41] F. B. Li, X. Z. Li, *Appl. Catal. A* **2002**, *228*, 15–27.
[42] H. Tang, H. Berger, P. E. Schmid, F. Levy, G. Burri, *Solid State Commun.* **1993**, *87*, 847–850.
[43] M. Anpo, N. Alkawan, Y. Kubokaway, *J. Phys. Chem.* **1985**, *89*, 5017–5021.
[44] S. Shamaila, A. K. L. Sajjad, F. Chen, J. Zhang, *Appl. Catal. B Environ.* **2010**, *94*, 272–405.
[45] M. Kruk, M. Jaroniec, *Chem. Mater.* **2001**, *13*, 3169–3183.
[46] C. H. Wang, C. L. Shao, Y. C. Liu, L. N. Zhang, *Scripta Mater.* **2008**, *59*, 332–335.
[47] J. H. Xin, S. M. Zhang, G. D. Qi, X. C. Zheng, W. P. Huang, S. H. Wu, *React. Kinet. Catal. Lett.* **2005**, *86*, 291–298.
[48] H. Li, D. Wang, P. Wang, H. Fan, T. Xie, *Chem. Eur. J.* **2009**, *15*, 12521–12527.
[49] A. S. Prakash, C. Shivakumara, M. S. Hegde, L. Dupont, J.-M. Tarascon, *Mater. Res. Bull.* **2007**, *42*, 707–712.
[50] J. H. Pan, W. I. Lee, *Chem. Mater.* **2006**, *18*, 847–853.
[51] J. C. Dupin, D. Gonbeau, P. Vinatier, A. Levasseur, *Phys. Chem. Chem. Phys.* **2000**, *2*, 1319–1324.
[52] S. M. Prokes, J. L. Gole, X. Chen, C. Burda, W. E. Carlos, *Adv. Funct. Mater.* **2005**, *15*, 161–167.
[53] V. N. Kuznetsov, N. Serpone, *J. Phys. Chem. B* **2006**, *110*, 25203–25209.
[54] K. Ikarashi, J. Sato, H. Kobayashi, N. Saito, H. Nishiyama, Y. Inoue, *J. Phys. Chem. B* **2002**, *106*, 9048–9053.
[55] J. Sato, H. Kobayashi, Y. Inoue, *J. Phys. Chem. B* **2003**, *107*, 7970–7975.
[56] A. Hagfeldt, M. Gratzel, *Chem. Rev.* **1995**, *95*, 49–68.
[57] G. Colón, M. C. Hidalgo, J. A. Navıo, *Langmuir* **2001**, *17*, 7174–7177.
[58] J. J. Testa, M. A. Grela, M. I. Litter, *Environ. Sci. Technol.* **2004**, *38*, 1589–1594.
[59] B. Sun, E. P. Reddy, P. G. Smirniotis, *Environ. Sci. Technol.* **2005**, *39*, 6251–6259.

Received: April 26, 2010
Published online: October 18, 2010

